# Sensitive, High-Strain, High-Rate Bodily Motion Sensors Based on Graphene–Rubber Composites

Conor S. Boland,[†] Umar Khan,[†] Claudia Backes,[†] Arlene O'Neill,[†] Joe McCauley,[†] Shane Duane,[†] Ravi Shanker,[‡] Yang Liu,[‡] Izabela Jurewicz,[‡] Alan B. Dalton,[‡] and Jonathan N. Coleman[†],*

[†]School of Physics, CRANN and AMBER, Trinity College Dublin, Dublin 2, Ireland and [‡]Department of Physics, University of Surrey, Guildford GU2 7XH, Surrey, England

ABSTRACT Monitoring of human bodily motion requires wearable sensors that can detect position, velocity and acceleration. They should be cheap, lightweight, mechanically compliant and display reasonable sensitivity at high strains and strain rates. No reported material has simultaneously demonstrated all the above requirements. Here we describe a simple method to infuse liquid-exfoliated graphene into natural rubber to create conducting composites. These materials are excellent strain sensors displaying 10^4-fold increases in resistance and working at strains exceeding 800%. The sensitivity is reasonably high, with gauge factors of up to 35 observed. More importantly, these sensors can effectively track dynamic strain, working well at vibration frequencies of at least 160 Hz. At 60 Hz, we could monitor strains of at least 6% at strain rates exceeding 6000%/s. We have used these composites as bodily motion sensors, effectively monitoring joint and muscle motion as well and breathing and pulse.
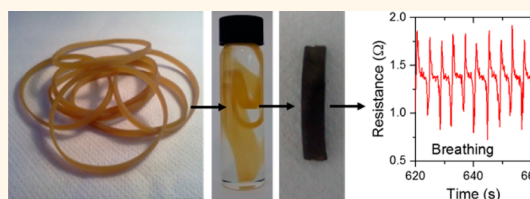
KEYWORDS: bodily motion sensors · graphene–rubber composites · strain sensors · dynamic strain

The past decade has seen a growing body of research devoted to the integration of electronics with biological or other soft, stretchable, flexible systems.[1] This field is broad, ranging from wearable biosensors[2] to ultralight, foldable plastic electronics.[3] An important subfield involves the development of devices or sensors to be mounted on or near the skin. Clearly, because of the soft, compliant nature of tissue and the natural bending or rotational motion associated with joints, many applications in this area will require the development of both structures and materials that can stretch, bend, fold, twist and generally deform in response to the motion of the wearer.[1,2,4] Such behavior is generally not compatible with traditional silicon/metal-based electronics. This has led to the development of various stretchable materials and structures, which have been used to fabricate a range of other devices including transistors and sensors, which can be integrated into clothing or worn directly on the skin.[5–9]

Increasing interest surrounds wearable biosensors,[10] which can monitor a range of biosignals including blood pressure, respiration rate and blood glucose levels.[2] Particularly important are wearable strain and motion sensors, which can be used to monitor joint and muscle motion with the aim of sensing posture, movement and even breathing.[4] A number of applications have been suggested: smart suits for babies, athletes or soldiers[4] or in monitoring of patients which are elderly, suffer from chronic disease or are in rehabilitation.[2,11]

Such sensors usually work by detecting the change in resistance of a material in response to variations in its length. However, wearable strain sensors have a range of requirements that are not all fulfilled by standard strain-sensing platforms. They need to be light and compliant, they must be sensitive enough to detect processes such as breathing, they should work at high strains to monitor large scale motion such as that associated with joints, and finally, they need to operate at high speeds/strain rates to follow fast voluntary and involuntary movement. In addition, it should be possible to produce the sensing material in various shapes, sizes and geometries, for example, as fibers that could be woven into garments. Ideally, these structures would

© 2014 American Chemical Society

also be cheap to produce to facilitate widespread availability. To the authors' knowledge no material combines all these properties, severely limiting our ability to fabricate multifunctional wearable strain and motion sensors.

This is unfortunate as sensors made from such materials could sense not only strain but velocity, acceleration and force. The resulting capabilities would facilitate applications not only in human motion sensing but also in a range of areas including monitoring of inflatable devices such as airbags, vibration detection and motion in robots or other moving mechanical objects.

In order to develop materials which can perform this array of functions, many researchers have turned to materials science and specifically nanotechnology. Strain sensors have been demonstrated from a range of materials and structures including hydrogels,[12] nanostructured papers,[13−15] graphene-woven fabrics,[11,16] nanotube arrays[9] and complex nanoengineered structures.[7] Particularly promising have been the nanocomposite strain gauges.[17] To date, strain gauges have been prepared from polymer-based composites, loaded with nanoparticles,[8] nanotubes,[17−22] graphene,[23−25] carbon nanofibers[17,26] and carbon black,[27,28] and have demonstrated performance far superior than those observed for commercial metal stain gauges.

The simplest performance metric is the gauge factor, G, which describes how the relative resistance change depends on strain, ε: $\Delta R/R_0 = G\varepsilon$. For a normal material with conductivity that is independent of strain, it can be shown (see Supporting Information (SI)) that, because of dimensional changes:

$$\frac{\Delta R}{R_0} = \varepsilon(2 + \varepsilon) \tag{1a}$$

For traditional strain gauges made of metal, this means $G \sim 2$ at low strain.[29] For some materials, such as composites, the conductivity is strain-dependent. Then, at low strain, we can relate the fractional resistance change to the strain by[29]

$$\frac{\Delta R}{R_0} = (1 + 2\nu)\varepsilon + \frac{\Delta\sigma(\varepsilon)}{\sigma_0} \tag{1b}$$

where the first term describes the effects of dimensional changes, while the second term describes the effects of any strain dependence of the conductivity (ν is Poisson's ratio). We note that for a perfect incompressible material, $\nu = 1/2$, so eqs 1a and 1b are consistent at low strain. In a nanocomposite, application of strain can change the spacing between conductive filler particles resulting in large resistivity changes. As a result, values of G as high as 1000 have been demonstrated, although the vast majority of papers report $G < 50$ (see SI for detailed literature review). Some results have been extremely impressive. Networks of graphene on elastomeric substrates have

demonstrated high gauge factor and good dynamic performance at strains as high as 8%.[16] Metalized polymer nanofibers have been fabricated into low-strain sensors for pressure, shear and torsion with good dynamic response up to 10 Hz.[7] Yamada et al. used arrays of carbon nanotubes to prepare high-strain sensors with very impressive dynamic response but relatively low gauge factor.[9] However, to the authors' knowledge, no reports exist for strain sensors that combine low stiffness, high gauge factor, high-strain and fast dynamic motion sensing capabilities with the potential for simple, cheap fabrication. This is an important gap that needs to be filled for strain sensors to fulfill their full potential.

We believe graphene to be a very promising filler mater for nanocomposite strain sensors. Currently one of the most studied of nanomaterials, graphene consists of atomically thin nanosheets of hexagonally bonded carbon.[30,31] These nanosheets display excellent electrical properties, can be produced in large quantities by liquid exfoliation[32,33] and are easily incorporated into polymers to form composites.[34] In this work we demonstrate a very simple method to infiltrate store-bought elastic bands with liquid-exfoliated graphene to produce versatile strain sensors. We show these simple strain sensors to work very well at strains of >800%, both under quasi-static conditions or at dynamic strain rates of at least 7000%/s. We also demonstrate impressive performance as kinesthetic motion sensors, detecting motions as subtle as those associated with breathing and pulse.

RESULTS

Infusion of Graphene. Preparation of graphene-infiltrated elastic bands (G-bands) requires two main steps: liquid exfoliation of graphene and infusion of graphene into the rubber. We first prepared dispersions of graphene in the solvent N-methyl-pyrrolidone (NMP) using well-known liquid exfoliation techniques.[32,35,36] Such processes give large quantities of unoxidized, defect-free graphene flakes (Figure 1 A,B) with lateral size of 500−1500 nm (Figure 1C) and typically 1−6 monolayers per flake.[32,36] We then soaked natural rubber-based, store-bought elastic bands (Figure 1D) in toluene. Because the solubility parameters of natural rubber and toluene are reasonably close (see SI), soaking results in considerable swelling[37] of the band (Figure 1E) with all dimensions increasing by factors of ×1.5−1.6 after 3.5 h soaking (Figure 1F,G). Natural rubber consists of aggregated latex particles with sizes from 100s of nm to microns. It is likely that these particles are poorly cross-linked allowing toluene to diffuse between them to create relatively large interparticle pores. The swollen bands were then transferred to a dispersion of graphene in NMP, to which water had been added such that the NMP:water ratio was 20:80. The presence of the water makes it energetically favorable for the graphene to migrate from the dispersion into the pores in the rubber
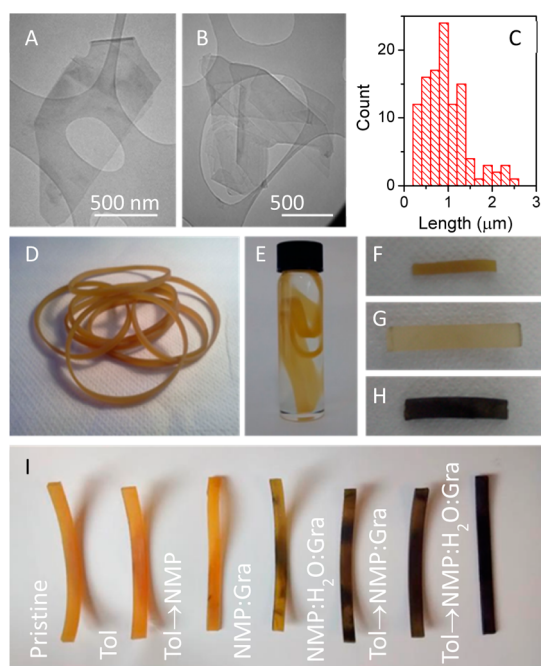
Figure 1. Preparation of graphene and graphene infused elastic bands (G-bands). (A,B) TEM images of typical few-layer graphene nanosheets produced by liquid exfoliation of graphite in NMP. (C) Histogram showing length of liquid exfoliated graphene nanosheets. The mean length was 1 μm. (D) As-bought elastic bands. (E) Elastic band while soaking in toluene. (F—H) A section of (F) an untreated rubber band, (G) a band section after soaking in toluene for 3.5 h and (H) a graphene-infused band prepared by swelling in toluene then soaking in an NMP:water:graphene mixture for 4 h followed by washing and drying. (I) Photograph of bands soaked under different conditions as described in the labels. The labeling can be understood as follows: the → represents a transfer from one liquid to another, while a colon separates the components of a mixture. Thus, "NMP:Gra" means the band was soaked only in a mixture of NMP and graphene, while "Tol → NMP:H$_2$O:Gra" means the band was first soaked in toluene before transferring to a dispersion of NMP, water and graphene. In all cases the toluene soak time was 3.5 h, while the soak time in NMP-based dispersions was 1 h. The NMP:H$_2$O ratio was 20:80, while the graphene concentration was 1 mg/mL. Note, only the "Tol → NMP:H$_2$O:Gra" treatment gave a uniform graphene coating/infusion.

that had been opened up by exposure to the toluene (see SI). Extensive washing (to remove any graphene adhered to the surface) and drying results in graphene-infused bands (Figure 1H). Note that all steps in this process are necessary to achieve good quality G-bands (Figure 1I).

The bands were soaked in the NMP:water:graphene dispersion for times ranging from 15 min to 48 h after which they were removed and washed. After through drying, the mass uptake of graphene was measured by careful weighing. This was converted to mean graphene volume fraction, ϕ, which is plotted versus soak time, t_s, in Figure 2A. The volume fraction scales as $\phi \propto \sqrt{t_s}$, reaching ~0.55 vol % after 48 h. The square-root time dependence indicates that the graphene uptake is diffusion-limited, which is consistent with
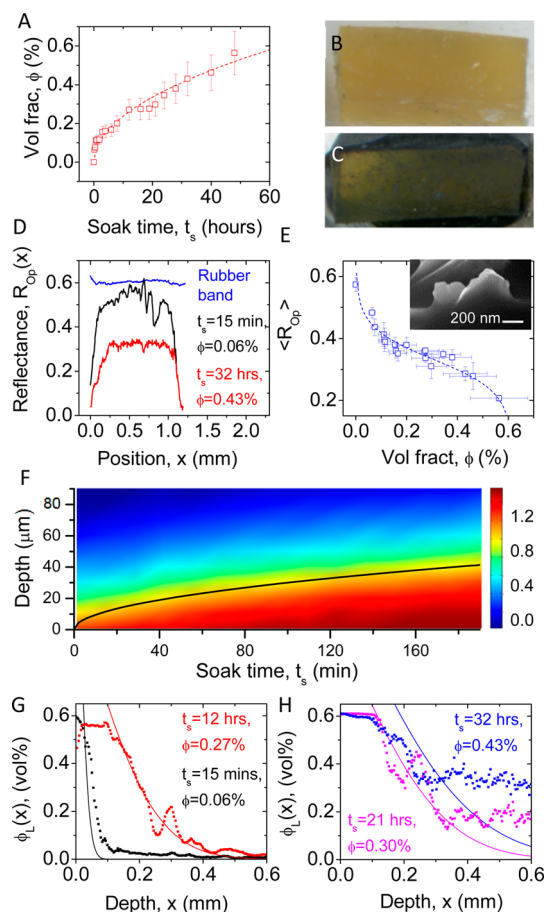

Figure 2. Characterization of G-bands. (A) Measured graphene content (vol %, after washing) as a function of soak time, t_s. The dashed line represents diffusion limited behavior (i.e., $\propto \sqrt{t_s}$). (B,C) Scanned images of freeze-fracture surfaces of G-bands after swelling in toluene followed by (B) soaking in NMP and (C) soaking in 20% NMP/water mixture for 48 h. (D) Local reflectance measured as a function of position on fracture surface (from top of band to bottom) plotted for a pristine band and two different G-bands. (E) Mean fracture surface reflectance as a function of graphene volume fraction. The dashed line shows an analytic, empirical relationship between $\langle R_{op} \rangle$ and ϕ (see SI for equation). Inset: Helium ion micrograph showing rubber-coated graphene flakes protruding from a band fracture surface. (F) NMR imaging was used to probe the concentration of NMP molecules bound to the surface of graphene nanosheets as a function of depth (y-axis) and soak time (x-axis). The color coding represents the concentration of NMP bound to graphene (proportional to concentration of graphene) in arbitrary units. The solid line represents a constant concentration profile consistent with depth $\propto \sqrt{t_s}$. (G,H) Local volume fraction, plotted as a function of depth. The solid lines are calculated using eq 2, while the data points are estimated from the reflectance data using the empirical relationship between $\langle R \rangle$ and ϕ described above. Note that a depth of 0.6 mm represents the center of the band. The theoretical curves in G and H were scaled to represent the actual local ϕ by first plotting in arbitrary units and then normalizing by multiplying by $\langle \phi_{exp} \rangle \times 0.6$ mm/$\int_0^{0.6mm} \phi_{theory}$ dx.

the graphene entering the interior of the band rather than solely adsorbing on the surface.[38] Quantitative analysis gives an upper limit for the diffusion coefficient for graphene within the rubber: $D < 2.5 \times 10^{-12}$ m^2/s

(see SI and ref 39). As expected, this is considerably lower than the diffusion coefficient for small molecules in rubber (>10^{-10} m^2/s).[40]

To confirm the infusion of graphene, we freeze-fractured a number of bands, allowing the examination of their interiors. Shown in Figure 2B,C are two images, recorded using a transmission scanner, of the fracture surfaces of two elastic bands. Each was swollen in toluene, however one was then transferred to an NMP:water mixture (*i.e.*, no exposure to graphene, Figure 2B), while the other was then soaked in an NMP:water:graphene mixture for 48 h ($\phi = 0.56$ vol %, Figure 2C). It is clear from the second image that the graphene has infused right to the center of the band resulting in a considerable darkening of the rubber. We can use the scanner to estimate the optical reflectance, R_{op}, of the G-band as a function of position across the fracture surface (*i.e.*, top to bottom in Figure 2B,C). This data is presented in Figure 2D (see SI for all data) and shows that for pristine bands $R_{op} \sim 0.6$, invariant with depth. For composite bands the reflectance in the interior of the band was always <0.6. Critically, for all composites, R_{op} increased from edge to center consistent with graphene content decreasing with depth into the band. This shows that while the graphene clearly diffuses deep into the bands, the graphene profile is not uniform and varies with soak time. Figure 2E shows the mean reflectance, $\langle R_{op} \rangle$, to fall smoothly with ϕ, consistent with a steady increase in graphene content with increasing soak time. The dashed line represents an empirical relationship between $\langle R_{op} \rangle$ and ϕ, which can be used to transform local R_{op} data to represent local volume fraction, ϕ_L (see SI and below). We can confirm the presence of graphene deep within the band by characterizing the fracture surface microscopically. Shown in Figure 2E (inset) is a He ion micrograph showing graphene sheets protruding from the rubber, confirming infusion deep into the interior.

We can dynamically probe the ingress of the graphene into the rubber using nuclear magnetic resonance (NMR) imaging. NMR probes the resonant frequency of proton nuclei in the magnetic field gradient as a function of depth into the band with the acquired signal reflecting the local proton density weighted by molecular mobility. Using NMR, chemical shift selection enables the observation of solvent components independently. Thus, a typical measurement gives the relative concentration of a given species as a function of depth within the rubber at a given time. A sequence of measurements taken over a given time period can be combined to give a map of concentration as a function of both depth and time. We monitored the infusion of graphene into rubber by placing a drop of NMP:water:graphene mixture on the surface of a toluene-swelled elastic band. NMR imaging showed two signals associated with NMP, which we attribute to free molecules and molecules bound to the graphene surface. Shown in Figure 2F is a typical map, which monitors the diffusion of graphene-bound NMP into the rubber. Here, the color-coded local volume fraction is plotted *versus* depth (*i.e.*, distance diffused into the rubber) and soak time. It is clear from this map that the depth where a given ϕ is observed (*e.g.*, $\phi = 1$ au) increases as $\sqrt{t_s}$ (solid line). This indicates a Fickian diffusion process.[40] The local concentration can be related to both depth, x, and soak time, t_s, by[41]

$$\phi_L(x) \propto \text{erfc}[x/(4Dt_s)^{1/2}] \qquad (2)$$

where erfc represents the complementary error function. Fitting gives a diffusion coefficient of $D = 4 \times 10^{-13}$ m^2/s, consistent with the values given above (see SI). It should be noted that the diffusion coefficient for free NMP was much faster: $D \sim 5 \times 10^{-12}$ m^2/s. However, this is slow relative to the literature value for toluene diffusion in rubber given above. This is probably because the solubility parameters of NMP and rubber are significantly different, hindering the ingress of free NMP (see SI).

Plotted in Figure 2E is an empirical function describing the relationship between $\langle R_{op} \rangle$ and ϕ (see SI). We can use this to estimate the local graphene volume fraction as a function of depth from reflectance line scans such as those shown in Figure 2D. Such data is shown for selected soak times in Figure 2G,H (see SI for all data). Also shown are the local volume fraction profiles calculated using eq 2 with $D = 4 \times 10^{-13}$ m^2/s. For $t_s \leq 12$ h, data from both the model and the reflectance measurements are in good agreement (Figure 2G). In particular, both show very small ϕ_L in the band center. However, for $t_s \geq 16$ h the agreement was much poorer (Figure 2H). Interestingly, for these longer times, the reflectance data showed more graphene than expected in the center of the band (see SI). We suggest that this may be due to the relatively broad nanosheet size distribution shown in Figure 1C. For long soak times, smaller flakes, which should have larger than average diffusion coefficients, travel deeper into the band leaving the larger flakes closer to the surface. Ultimately this means that for soak times below $\sim$12 h, the graphene is present as a surface layer, while for t_s above 21 h, it is distributed much more uniformly.

Properties of G-Bands. For each of the soak times, we measured the (unstrained) electrical resistance, R_0, as a function of graphene volume fraction (Figure 3A). The resistance varied from 4 MΩ at very low volume fraction ($\phi = 0.06$ vol %, $t_s = 15$ min) to 57 kΩ at $\phi = 0.56\%$ ($t_s = 48$ h). To better understand this, we plot the G-band conductivity, σ, as a function of volume fraction in Figure 3B. The conductivity increases from 10^{-3} S/m for the lowest volume fraction to $\sim$0.1 S/m for $\phi = 0.56\%$. Interestingly, this data clearly shows a kink at $\phi \approx 0.3\%$ that separates two regimes, at higher and lower ϕ respectively. This behavior is reproducible and has been observed in multiple batches of G-bands (see SI). This kink occurs for bands prepared with soak
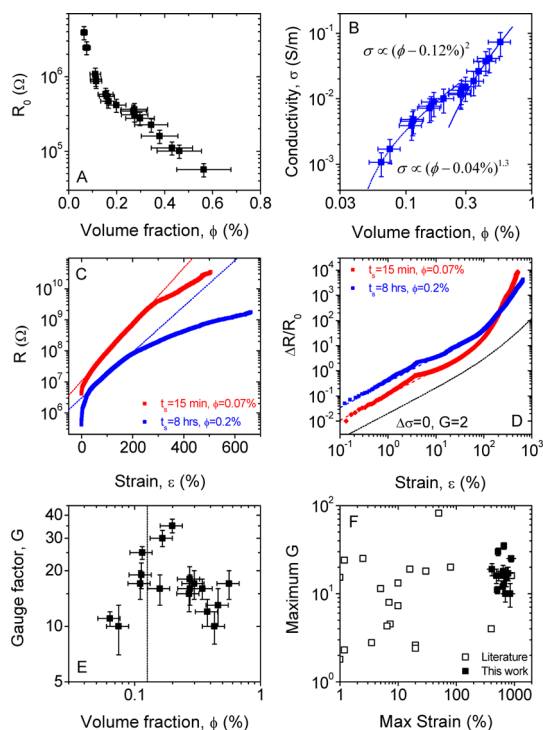
Figure 3. Electrical properties of G-bands. (A) Measured resistance at zero strain, R_0, plotted *versus* graphene volume fraction, ϕ. **(B)** Conductivity of bands plotted as a function of graphene volume fraction. The lines are fits to percolation theory. The upper region (solid line) was described by a percolation threshold. $\phi_{c,U} = 0.12\%$ and exponent $t = 2$ and is consistent with transport through the bulk of the band. The lower region (dashed line) was described by $\phi_{c,L} = 0.04\%$ and $t = 1.3$ and is consistent with transport along the surface of the band. **(C)** Measured resistance as a function of applied strain for bands for two different soak times. **(D)** Plots of $\Delta R/R_0$ *versus* strain (log−log scale). The dashed lines show the linear region as defined by $\Delta R/R_0 = G\varepsilon$. The solid line shows what would be expected if the resistance change was solely due to dimensional changes on stretching (*i.e.*, $\Delta\sigma = 0$). **(E)** Gauge factor, G, plotted *versus* graphene volume fraction. The dashed line represents the bulk percolation threshold (0.12%). **(F)** Summary of results reported in the literature for nanocomposite strain sensors (see Table S2 (SI)). The maximum reported value of G plotted *versus* the maximum reported strain. Also plotted are the results obtained in this work.

times between 12 and 19 h. This is exactly the range where the graphene transitions from being localized close to the surface to being more uniformly distributed (Figure 2 G,H). This will be discussed in more detail below.

The electrical properties of composites consisting of a conductive filler in an insulating matrix are generally described by percolation theory.[42] In such systems, current can only flow above a critical volume fraction, the percolation threshold, where the first continuous conducting path across the matrix is formed. Above the percolation threshold the conductivity is described by the percolation scaling law:

$$\sigma = \sigma_0 (\phi - \phi_c)^t \qquad (3)$$

where ϕ_c is the percolation threshold, t is the percolation exponent and σ_0 is usually similar to the

conductivity of the filler when formed into a film.[43] We will treat the two regimes described above separately, first fitting eq 2 to the data with $\phi > 0.3\%$ (*i.e.*, $t_s \geq 21$ h) and then separately to the data for $\phi < 0.25\%$ (*i.e.*, $t_s < 12$ h). In the upper regime, a good fit (solid line) is found for $\phi_{c,U} = 0.12\%$ and $t = 2$. The percolation threshold is close to literature values[44] and consistent with the value of $\phi_c \sim 0.1\%$ expected theoretically for isotropic distributions of nanosheets with aspect ratio ~ 1000.[45] The percolation exponent is identical to the universal value of 2.0 expected for transport in 3-dimensions.[42] This is consistent with the data in Figure 2H, which suggests that for the higher soak times, the graphene is distributed throughout the G-band. Interestingly the fit gives $\sigma_0 = 3700$ S/m, very close to the expected conductivity value for films of liquid exfoliated graphene.[46,47] This implies that the graphene flakes making up the conducting network are in close contact with no evidence of the polymer coatings that usually limit the conductivity of nanocomposites.[48]

We have also fit eq 3 to the lower range ($\phi < 0.25\%$). We find a very good fit for $\phi_{c,L} = 0.04\%$ and $t = 1.3$ (dashed line). This is extremely interesting as 1.3 is the universal percolation exponent for transport in 2 dimensions.[42] This implies that in the volume fraction range $\phi < 0.25\%$, the dominant mode of conduction is through the graphene close to the surface. Again, this is consistent with the data in Figure 2G, which shows the graphene to be largely localized in a surface layer for the shorter soak times. It is worth noting that when analyzing conductivity in a surface layer, eq 3 might seem inappropriate. However, electrical properties of thin films of conducting nanomaterials are known to be well described by $\sigma \propto (N_A - N_{A,c})^t$ were N_A is the nanoconductor areal number density (effectively the thickness of the layer of nanoconductors) and $N_{A,c}$ is the associated percolation threshold.[42] Because $N_{A,c} \propto \phi$, eq 3 can be used to fit the low ϕ data as well as the high ϕ regime. We then attribute $\phi_{c,L} = 0.04\%$ as the mean volume fraction for which the first surface conducting path forms. Extrapolation of the data in Figure 2A implies this first path to occur after a soak time of ~ 5 min under the conditions used in this work.

The electrical data implies that G-bands can be thought of as two resistors in parallel, one representing the graphene-rich layer close to the surface and the other representing the graphene in the bulk of the band. For volume fractions above $\phi \sim 0.3\%$ the current flowing through the bulk dominates, while for $\phi < 0.25\%$, current flowing in the surface layer is dominant.

Strain Sensing. Natural rubber is an extremely extensible material:[49] mechanical testing showed the pristine rubber bands to have strains-at-break of $\sim 1100\%$. This was not significantly reduced by swelling in toluene followed by soaking in NMP:water (see SI).

While the infusion of graphene did reduce the strain at break somewhat, composite bands could be strained to 500−1100% before failure (see SI).

This makes these materials potentially useful as high-strain strain sensors. Whether the dominant current flows through graphene nanosheets near the surface or in the bulk, we expect the electrical resistance to increase on the application of strain due to the divergence of adjacent nanosheets. We slowly applied strain (dL/dt =10 mm/min) to G-bands with a range of volume fractions (unstrained length, L_0 = 15 mm). Note the experiment was set to stop before breaking, meaning that the maximum strains observed are lower limits. Two examples of the resultant resistance-strain curves are shown in Figure 3C (all others are shown in the SI). In all cases the resistance increased dramatically on the application of strain. Although the curves followed no single trend, in all cases an exponentially increasing region was observed at low to intermediate strains (∼5% to 100−300% depending on ϕ). We fit this region to $R = R_0 e^{\varepsilon/\varepsilon_0}$ (dashed lines), finding values of ε_0 in the range 25−100%. Although ε_0 tended to fall with increasing volume fraction, the data was very scattered (see SI). Such exponential behavior has been observed before for nanocomposite strain sensors[50,51] and has been explained as being due to the exponential decrease in interparticle tunnelling probability with strain.[20,50−53] Within such frameworks, ε_0 is a parameter that is related to the height of the potential barrier between nanoparticles. Previously reported sensors based on polymer/carbon-fiber[50] composites and polymer/nanotube[51] composites displayed data consistent with values of ε_0 of ∼2% and ∼15% respectively.

The fractional resistance change ($\Delta R/R_0$) is plotted versus strain for two samples in Figure 3D (all data is shown in the SI). Resistance changes as large as $\times 10^4$ were observed for strains of $\varepsilon > 700\%$ (see SI, t_s = 12 h). Also plotted on Figure 3D is the behavior expected for a material with strain-independent conductivity such that the resistance increase is solely due to dimensional changes (dashed line). This is described by eq 1a and is equivalent to $G = 2$. For all our samples, the resistance changes are well above this line. This means that, in addition to dimensional changes, strain-induced changes in conductivity play an important role in these sensors. For all samples, we found $\Delta R/R_0$ to scale linearly with ε once $\varepsilon < 4\%$ (Figure 3D and SI), allowing the calculation of G (Figure 3E). The gauge factor increases with decreasing volume fraction from $G \sim 10$ for composites with $\phi \sim 0.5\%$ to a maximum value of $G = 35$ for a G-band with $\phi = 0.2\%$, very close to the bulk percolation threshold (0.12%). Below the bulk percolation threshold, where electrical transport is predominantly along the surface of the bands, G falls considerably reaching $G = 10-15$ for $\phi = 0.07\%$. This suggests that elastomers coated with graphene do not make good strain sensors. Rather, bulk composites

with graphene content close to the percolation threshold are required.

The maximum observed gauge factor of $G = 35$ is relatively high compared to values reported in the literature (Table S2 (SI)). In addition, G-bands can be stretched to strains that are extremely high compared to most reported strain sensors. To compare these values to the literature, we plot a map of the maximum reported values of both G and the maximum operating strain for a range of nanocomposite strain sensors from both the literature and the study described here (Figure 3F and Table S2 (SI)). We find the best G-band strain sensors to have comparable gauge factors to the best high-strain sensors. However, G-bands described here work at considerably higher stains than all but the most extensible strain sensors reported to date.

Dynamic Sensing. The combination of sensitivity and extensibility (Figure 3F) suggests G-bands to be ideal for dynamic strain sensing. To test this, we used a tensile tester to subject G-bands prepared with a range of soak times to a cyclic strain profile (Figure 4A,B). The strain wave was trapezoidal in shape with a frequency of 0.33 Hz. The minimum strain was 5%, while the maximum strain was 75% giving a maximum strain rate of 140%/s. In all cases, $\log(R)$ followed the strain extremely well (Figure 4A,B and SI). The fractional resistance change over the cycle, $(R_{max} - R_{min})/R_{min}$, is plotted versus graphene volume fraction in Figure 4C. This data is very similar to that in Figure 3E and shows the dynamic response to be maximized for volume fractions just above the bulk percolation threshold. The t_s = 12 h ($\phi = 0.27\%$) sample displayed $(R_{max} - R_{min})/R_{min} = 100$ for $\varepsilon_{max} = 75\%$. This is competitive with the best nanocomposite strain sensors which operate at strains above 1%.[8,9,16] For comparison, Park et al. demonstrated silver nanoparticle/elastomer composites that operated at 1 Hz displaying maximum values of $(R_{max} - R_{min})/R_{min} = 3$ at strains up to 16% .[8] As with most nanocomposites,[54,55] some conditioning is generally observed, here over the first 200 cycles (Figure 4D and SI). However, after 200 cycles the response is extremely stable.

In these experiments, the frequency was limited by the tensile tester used. To explore the sensor response at higher frequencies we used a commercial vibration generator to drive a piston that oscillated the band perpendicular to its length (Figure 4E). Using a traveling microscope we could show that, with the band in place, the piston oscillated like a damped, driven linear oscillator with amplitude, y_{amp}, which varied with frequency, ν, as $y_{amp} = y_{res}\gamma\nu/[(\nu^2 - \nu_0^2)^2 + (\gamma\nu)^2]^{1/2}$ where $y_{res} = 3.0$ mm was the resonant amplitude, $\gamma = 22$ Hz was the damping constant and $\nu_0 = 63.5$ Hz was the resonant frequency (see SI). In this geometry and at low strain, the strain amplitude is given by $\varepsilon_{amp} \approx 2y_{amp}^2/L_0^2$. Using an oscilloscope we monitored the amplitude of resistance oscillation, ΔR_{amp}, as a function
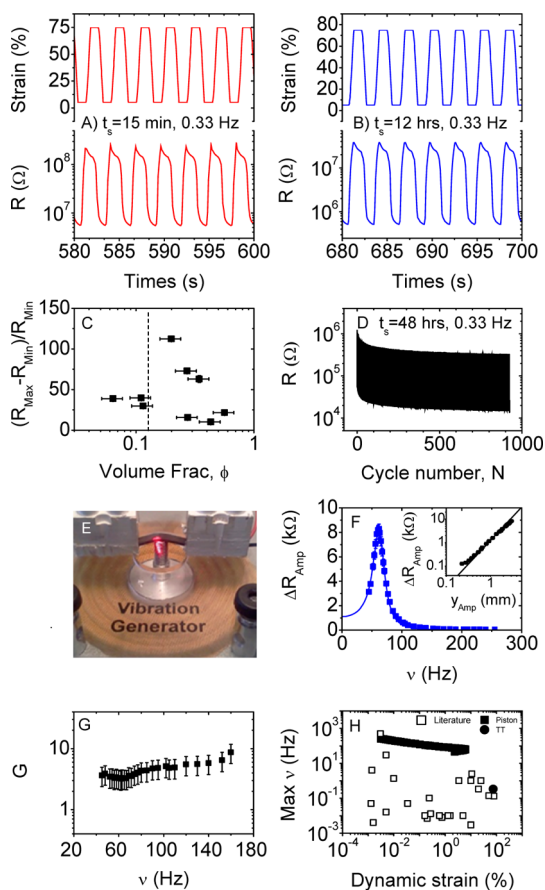
Figure 4. Dynamic motion sensing using G-bands. (A,B) Resistance change as a response to cyclic strain for bands prepared with soak times of 15 min ($\phi = 0.06$ vol %) and 12 h ($\phi = 0.27$ vol %). In both cases the strain wave was trapezoidal in shape with a period 3 s (rise and fall times of 0.5 s and time at max and min 1 s). The minimum strain was 5%, while the maximum strain was 75%. **(C)** Fractional resistance change on cycling plotted *versus* volume fraction, ϕ. The dashed line represents the bulk percolation threshold, $\phi_{c,U} = 0.12\%$. **(D)** Resistance data plotted *versus* cycle number for a band prepared with soak time of 48 h ($\phi = 0.56$ vol %). **(E)** Photograph of a mounted G-band about to be driven to oscillate perpendicular to its length by a vertically vibrating piston. **(F)** Frequency dependence of the peak to peak resistance change, ΔR_{amp}. The line represents the behavior expected for a damped driven piston with the resistance amplitude proportional to the square of the piston amplitude (see text). Inset: Peak to peak resistance change plotted *versus* piston displacement amplitude. The line demonstrates that $\Delta R_{amp} \propto y_{amp}^2$. **(G)** Dynamic gauge factor, G, plotted *versus* vibration frequency. **(H)** Survey of the literature for dynamic strain sensing with composites. The open symbols represent nanocomposite sensors reported in the literature (see Table S2 (SI)). The closed symbols represent the piston and tensile tester (TT) data from this work.

of frequency as shown in Figure 4F. Because $\Delta R = G R_0 \varepsilon$ at low strain, the resistance amplitude is expected to be given by

$$\Delta R_{amp} \approx 2 R_0 G y_{amp}^2 / L_0^2 \qquad (4)$$

As such we fit the data in Figure 4F to

$$\Delta R_{amp} = \frac{\Delta R_{res}(\gamma \nu)^2}{[(\nu^2 - \nu_0^2)^2 + (\gamma \nu)^2]} \qquad (5)$$

(*i.e.*, $\propto y_{amp}^2$) where $\Delta R_{res} = 7.8$ kΩ is the resistance amplitude on resonance and $\gamma = 24$ Hz and $\nu_0 = 63.8$. We note that the fit is very good over all frequencies, even close to resonance where the G-band is subjected to tensile velocities (*i.e.*, dL/dt), tensile strains and strain rates of approximately 35 cm/s, 6% and 7000%/s, respectively. We plot ΔR_{amp} *versus* y_{amp} in Figure 4F (inset) showing behavior predicted by eq 4. The calculated gauge factor is plotted *versus* frequency in Figure 4G showing approximate frequency independence. We note that the sensitivity of this G-band remains undiminished at frequencies of up to 160 Hz. We compare our dynamic results to the literature in Figure 4H (literature data open symbols). We found G-bands to work at higher combinations of frequency and strain than any other composite strain sensor.

Kinesthetic Sensing. We believe G-bands to be of great interest in a range of applications but in particular as components in medical devices for measuring human (or animal) bodily motion. To demonstrate the broad dynamic range of the G-bands, we tested them as strain sensors in a number of scenarios. By attaching a G-band across the first knuckle of the index finger (Figure 5A) we could monitor the relatively high-strain motion ($\varepsilon \sim 40\%$) associated with repeated bending of the finger (Figure 5B). We could detect muscular motion associated with clenching and unclenching of the fist ($\varepsilon \sim 4\%$) by wrapping a G-band around the forearm (Figure 5C,D). By attaching the G-Band to the throat (Figure 5E) we could detect speech (Figure 5F). However, the G-band is so sensitive that if the subject did not remain still, small neck movements dominated the response, rendering the throat movement associated with speech undetectable.

We also attempted to measure the very subtle motions associated with breathing and pulse. To monitor breathing, a ~4 cm long G-band was attached horizontally across the rib cage on the subjects side. The resistance was monitored over approximately 5 min with the subject sitting in a chair. Figure 5G shows the resistance-time waveform to be well-defined and periodic response but also asymmetric. The Fourier transform (Figure 5H) clearly shows the Fourier components associated with the breathing movement. To measure pulse, a band was wrapped around the tip of the subject's finger (~20% prestrain) as a pulse sensor. Under these circumstances, a symmetric, periodic waveform was detected (Figure 5I) with a single Fourier component of frequency ~1 Hz (Figure 5J), as expected for human pulse.

Finally, it is worth considering the safety of graphene based strain sensors that might be worn near the skin. First, we note that recent *in vitro* tests in our lab have shown liquid exfoliated graphene to display virtually no toxicity toward human cells.[56] Nevertheless, we decided to explore the possibility of graphene being transferred from the G-band to the skin,
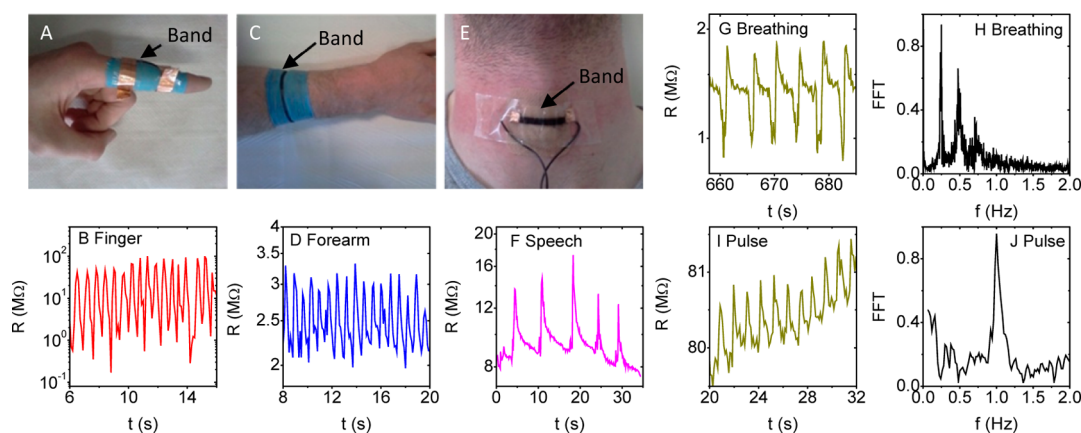
Figure 5. Applications of G-bands as body monitors. (A) Photo of a G-band connected across a knuckle and **(B)** resistance trace as the finger is repeatedly bent. **(C)** Photo of a G-band wrapped around a forearm and **(D)** resistance trace as the hand is repeatedly opened and closed. **(E)** Photo of a G-band attached to a throat and **(F)** resistance trace as the word "graphene" is repeatedly spoken. **(G)** Resistance traces showing slow breathing. **(H)** Fast Fourier transform showing Fourier components of the breathing waveform. **(I)** Resistance traces showing pulse. **(J)** Fast Fourier transform showing Fourier components of the pulse waveform.

specifically in the presence of sweat. To do this, we sonicated G-bands in human sweat, carefully weighing the band before and after sonication. On average, we found a relative mass loss of $(1.5 \pm 0.75) \times 10^{-3}$. This suggests that under very extreme conditions, some of the graphene may detach from the G-band. However, in real world applications, this could be mitigated by encapsulation of the G-band using an appropriate barrier polymer.

DISCUSSION

The G-band strain sensors described in this work have four main strengths. The process is potentially cheap and scalable. Liquid-exfoliated graphene can be produced in large quantities[33] and will be cheap compared to most nanomaterials. We envisage graphene infusion occurring during rubber production with very little process modification. In addition, the sensitivity of these materials is relatively high for a composite strain sensor ($G = 35$), making them competitive with most commercial strain sensors. More importantly, these strain sensors are the most extensible ever demonstrated, performing beyond 800% strain. This extensibility facilitates the monitoring of dynamic strain, allowing their use as velocity and acceleration sensors. Indeed this may be their greatest strength: these sensors operate at combinations of frequency and strain amplitude, unheard in any other strain sensors (*e.g.*, 60 Hz and 6% strain). Moreover, it is worth noting that the dynamic data we have reported represent lower performance limits as the strains and frequencies applied were limited by the equipment and not the G-bands.

These strain sensors display a number of advantages over other nanocomposite strain sensors prepared using fillers such as carbon black, carbon nanotubes, carbon nanofibers or nanographite. First, we believe

there is a significant advantage to the production method. Nanocomposite strain sensors are generally made by solution- or melt-processing during which the nanofillers tend to get coated by a layer of polymer. This can result in significant reductions[48] in the σ_0 parameter eq 3 meaning that relatively high loading levels are required to obtain a resistance appropriate for practical measurements. Such high loading levels may be undesirable as they can degrade other composite properties such as extensibility.[57] In our method, the graphene enters the polymer by diffusion through the internal porous structure, resulting in a network of well-connected flakes with no interflake polymer layers. The resultant nanocomposites have high values of σ_0, allowing reasonably small resistances to be achieved for relatively low graphene loading. Importantly, the process is universal and will allow the addition of other nanomaterials.

In addition, we believe that graphene as a material offers certain advantages. As described above, nanocomposite strain sensors should display a reasonable conductivity at low loading level. To minimize the percolation threshold,[45] large aspect ratio nanofillers are usually preferable. Nanographite particles typically display aspect ratios smaller than those associated with graphene leading to percolation thresholds well above 1%.[52,58] While carbon nanotubes have large aspect ratios and have been used to produce composites with low percolation thresholds,[48] nanotubes are expensive, making most composite applications economically unviable. Carbon fibers have high aspect ratios, leading to percolation thresholds ~1%.[50,59] However, due to their relatively large dimensions, carbon fiber-filled elastomers tend to have very low extensibility,[60] making them unsuitable for high-strain applications. Carbon black (CB) is very cheap and under certain circumstances can give composites with percolation

thresholds as low as 1%.[58] However, in most cases CB/polymer composites have percolation thresholds >10%.[61−63] This means large volume fractions are needed to obtain the required resistances,[28] generally leading to extensibilities that are lower than in the neat polymer.[64] In contrast, the graphene-filled composites described here have a percolation threshold well below 1%, extensibilities approaching 1000% and are expected to be relatively cheap.

These advantages are reflected in the exceptional performance of these strain sensors that combine high sensitivity and high rate capability with the potential to work at high strain. They perform very well compared to the literature as shown in Figures 3F and 4H. This combination of properties makes these sensors ideal for a range of applications from vibration monitoring in the automotive or aerospace industry to kinesthetic (bodily motion) sensing in the medical devices industry. We believe they are particularly useful in the latter due to their lightweight nature, high compliance and the potential to form them into fibrous thread-like structures. One can envisage weaving G-band based sensors into clothing to monitor the motion of athletes or patients undergoing rehabilitation. Alternatively, they could be used as early warning systems for cot death in babies or diagnosis of sleep apnea in adults. Ultimately, one can imagine a wearable network of G-bands performing wellness monitoring by continuous recording of functions like breathing, heart rate and pulse. Indeed, such applications may be realistic specifically due to the extremely low cost of these sensors. A typical G-band contains ∼0.1 g of rubber and <1 mg graphene, making the materials cost essentially zero. This will make it possible to roll out G-band based sensors extremely widely, for example, facilitating use in the developing world.

CONCLUSION

In summary, we have demonstrated a very simple process for producing graphene−natural rubber composites. Addition of graphene results in electrical conductivities as high as 0.1 S/m and so electrical resistances of <100 kΩ. Critically, the resistance depends strongly on the strain allowing these composites to function as strain sensors. They are sensitive, displaying gauge factors of up to 35, and operate at high strains and strain rates, making them ideal for a range of applications in dynamic strain sensing.

METHODS

G-Band Preparation. A *County Stationary No. 32* elastic band (natural rubber based) was placed in a vial of toluene in a low power sonic bath (Branson 1510 model 42 kHz) for 3.5 h. Under these circumstances, the band swells to approximately four times its initial volume. A dispersion of graphene in NMP was prepared by ultrasonic tip-sonication (Sonics Vibra Cell model VCX, 750W, 42 kHz) for 72 h at 45% amplitude. This was then vacuum filtered to form a film that was redispersed at high concentration (5 mg/mL) by ultrasonic tip-sonication for 10 min followed by bath-sonication for 2.5 h.[65] Water was added to give a composition of NMP:water = 20:80 by volume (see SI for optimization of NMP:water ratio) and so an overall graphene concentration of 1 mg/mL. In the text, such dispersions are referred to as NMP:water:graphene. The toluene-treated rubber bands were then directly placed into this dispersion and soaked for various times from 15 min to 48 h. Critically, tests show the exfoliated graphene to be very stable for at least 48 h in these NMP:water mixtures and reasonably stable over 48 h in a mixture of NMP and toluene (see SI). After soaking, they were washed by bath sonication in deionized water for 45 min (see SI for optimization of washing time). After this treatment the rubber band was left to dry in an oven at 60 C for 72 h. Thermogravimetry showed virtually no evidence of any residual solvent remaining after drying in this way (TGA curves composites differed by no more than 0.3% in the region between 100 °C < T < 200 °C, see SI). It is worth noting that the bands are unaffected by soaking in NMP, water or NMP:water mixtures with no apparent dissolution or degradation. We have found that each step in this process (i.e., soaking in toluene followed by transfer to graphene:NMP:water) is necessary for the production of good quality G-bands.

The mass uptake of graphene was found using an accurate balance to measure the mass of the bands before and after soaking, taking due consideration of the mass lost due to the solvent treatment and cleaning. Mass fraction was converted to volume fraction taking $\rho_{gra} = 2200$ kg/m^3 and $\rho_{rubber} = 1000$ kg/m^3. Optical scans were made using an Epson Perfection V700 Photo flat-bed scanner with a bit depth of 48 bits per pixel and a spatial resolution of 6400 dpi. The scanner output (in reflective mode) was converted to reflectivity by scanning white and black objects to obtain outputs consistent with $R \sim 0$ and $R \sim 1$ and subsequently normalizing the signal. Helium ion microscopy was performed on film fracture surfaces with a Zeiss Orion Plus. The working distance was ∼5 mm and a 20 μm aperture was used. The beam current was 0.5 pA with a tilt of 15 degrees.

NMP imaging was performed using an open-access GARField benchtop permanent magnet, characterized by a magnetic field of 0.7 T and gradient strength G of 17.5 T/m in the vertical direction. The strong magnetic field gradient is generated by two shaped magnet pole pieces and encodes the spatial position to yield one-dimensional proton profiles through the sample with a maximum spatial resolution of <8 μm to a depth of approximately 750 μm into the rubber. A radiofrequency (RF) planar-spiral surface coil of 6 mm in diameter is located at the center of the pole gap and selects a comparable sample planar area. The RF coil has variable capacitors for tuning and matching, which are placed several coil diameters from the coil. Molecular mobility is expressed by the self-diffusivity along the gradient direction and by the NMR longitudinal and transverse relaxation times T_1 and T_2. These parameters describe the nuclear spin relaxation caused by molecular rotation, with T_2 affected by slower motional processes. For these experiments, the rubber bands were cut into 450−500 μm thick pieces, and then placed on the sample stage that is above the coil. The profile of a dry pristine sample was taken as a reference. The experiment was performed by depositing a drop of NMP:water:graphene mixture on the surface of a rubber band and using NMP to monitor the ingress of the graphene.

Electromechanical Testing. Samples for electrical and electromechanical testing were prepared by cutting the bands into 1.5 or 4 cm segments. Initially, we performed both 2- and 4-probe electrical measurements using a Keithley KE2601 source meter. In all cases both techniques gave the same resistance indicating the contact resistance to be very small compared to the band resistance. Subsequently, all measurements were made using 2 probes. A Zwick Z0.5 ProLine Tensile Tester (100 N Load Cell) was used to apply dynamic strain to the

band, while a Keithley KE2601 source meter, controlled by LabView software, was used to measure the electrical resistance of the band as a function of time. The bands were first strained slowly (10 mm/min) until they reached a preset resistance with stress, strain and electrical resistance monitored continuously. This was performed for bands that had been soaked for times from 15 min and 48 h. In addition, purely mechanical measurements were performed where the G-bands were stretched to failure (strain rate 10 cm/min).

Dynamic electromechanical testing was performed on bands soaked for a number of bands spanning the whole range of soak times. Trapezoidal strain-time profiles were applied as shown in Figure 4 with resistance and strain monitored as a function of time for 500−1000 cycles. High rate measurements were performed using a Philip Harris Vibration Generator, a Tektronix TDS3024 oscilloscope to measure the resistance amplitude and a traveling microscope to measure the vibration amplitude. The band used for the high frequency measurements had unstrained length and resistance: $L_0 = 4$ cm, $R_0 = 220$ kΩ.

Samples for the kinesthetic testing were prepared with bands soaked for 48 h. A band cut into ∼4 cm segment was taped to the first knuckle of the index finger, which was wrapped in a finger segment of nitro-cellulose lab glove, using conductive copper tape. A Keithley KE2601 source meter and crocodile clips were used to measure the change in resistance due to joint movement with time.

For the muscular motion detection a band was produced by soaking in the graphene dispersion with a short segment of the band raised above the surface of the liquid and so unexposed to the graphene. In this way, the entire band was conducting except for a short (∼1 cm) long insulating section. The cutoff wrist section of a nitro-cellulose lab glove was placed through the band and was pulled over the forearm. The crocodile clips and leads attached to the source meter were clipped directly to the band either side of the insulating section.

For speech, breathing, and pulse response an adhesive bandage was attach to the throat just below the thyroid cartilage, across the 5,6 and seventh rib and around the tip of the index finger, respectively. A ∼4 cm band segment in each case was wrapped around or put across the bandage. Wire leads were attached to the bands at either end with conductive copper tape, which were connected to the source meter, and held in place over the skin/bandage using household scotch tape during testing.

G-bands were sonicated in human sweat (obtained from a subject after jogging while wrapped in plastic) for 2 h using a sonic bath (Branson 1510) . The bands were then dried in a vacuum oven at 60 degrees for 24 h

Conflict of Interest: The authors declare no competing financial interest.

Supporting Information Available: Detailed methods and complete characterization data. This material is available free of charge *via* the Internet at http://pubs.acs.org.

REFERENCES AND NOTES

1. Rogers, J. A.; Someya, T.; Huang, Y. G. Materials and Mechanics for Stretchable Electronics. *Science* **2010**, *327*, 1603–1607.
2. Pantelopoulos, A.; Bourbakis, N. G. A Survey on Wearable Sensor-Based Systems for Health Monitoring and Prognosis. *Syst., Man, Cybern.* **2010**, *40*, 1–12.
3. Kaltenbrunner, M.; Sekitani, T.; Reeder, J.; Yokota, T.; Kuribara, K.; Tokuhara, T.; Drack, M.; Schwodiauer, R.; Graz, I.; Bauer-Gogonea, S.; *et al.* An Ultra-Lightweight Design for Imperceptible Plastic Electronics. *Nature* **2013**, *499*, 458–465.
4. Lam Po Tang, S. Recent Developments in Flexible Wearable Electronics for Monitoring Applications. *Trans. Inst. Meas. Control* **2007**, *29*, 283–300.
5. Lipomi, D. J.; Vosgueritchian, M.; Tee, B. C. K.; Hellstrom, S. L.; Lee, J. A.; Fox, C. H.; Bao, Z. N. Skin-Like Pressure and Strain Sensors Based on Transparent Elastic Films of Carbon Nanotubes. *Nat. Nanotechnol.* **2011**, *6*, 788–792.
6. Kim, D.-H.; Ahn, J.-H.; Choi, W. M.; Kim, H.-S.; Kim, T.-H.; Song, J.; Huang, Y. Y.; Liu, Z.; Lu, C.; Rogers, J. A. Stretchable and Foldable Silicon Integrated Circuits. *Science* **2008**, *320*, 507–511.
7. Pang, C.; Lee, G. Y.; Kim, T. I.; Kim, S. M.; Kim, H. N.; Ahn, S. H.; Suh, K. Y. A Flexible and Highly Sensitive Strain-Gauge Sensor Using Reversible Interlocking of Nanofibres. *Nat. Mater.* **2012**, *11*, 795–801.
8. Park, M.; Im, J.; Shin, M.; Min, Y.; Park, J.; Cho, H.; Park, S.; Shim, M. B.; Jeon, S.; Chung, D. Y.; *et al.* Highly Stretchable Electric Circuits from a Composite Material of Silver Nanoparticles and Elastomeric Fibres. *Nat. Nanotechnol.* **2012**, *7*, 803–809.
9. Yamada, T.; Hayamizu, Y.; Yamamoto, Y.; Yomogida, Y.; Izadi-Najafabadi, A.; Futaba, D. N.; Hata, K. A Stretchable Carbon Nanotube Strain Sensor for Human-Motion Detection. *Nat. Nanotechnol.* **2011**, *6*, 296–301.
10. Cherenack, K.; van Pieterson, L. Smart Textiles: Challenges and Opportunities. *J. Appl. Phys.* **2012**, *112*, 091301.
11. Tormene, P.; Bartolo, M.; De Nunzio, A. M.; Fecchio, F.; Quaglini, S.; Tassorelli, C.; Sandrini, G. Estimation of Human Trunk Movements by Wearable Strain Sensors and Improvement of Sensor's Placement on Intelligent Biomedical Clothes. *Biomed. Eng. Online* **2012**, *11*, 95.
12. Manandhar, P.; Calvert, P. D.; Buck, J. R. Elastomeric Ionic Hydrogel Sensor for Large Strains. *IEEE Sens. J.* **2012**, *12*, 2052–2061.
13. Li, X.; Levy, C.; Elaadil, L. Multiwalled Carbon Nanotube Film for Strain Sensing. *Nanotechnology* **2008**, *19*, 045501.
14. Kang, I. P.; Schulz, M. J.; Kim, J. H.; Shanov, V.; Shi, D. L. A Carbon Nanotube Strain Sensor for Structural Health Monitoring. *Smart Mater. Struct.* **2006**, *15*, 737–748.
15. Gullapalli, H.; Vemuru, V. S. M.; Kumar, A.; Botello-Mendez, A.; Vajtai, R.; Terrones, M.; Nagarajaiah, S.; Ajayan, P. M. Flexible Piezoelectric Zno-Paper Nanocomposite Strain Sensor. *Small* **2010**, *6*, 1641–1646.
16. Li, X.; Zhang, R. J.; Yu, W. J.; Wang, K. L.; Wei, J. Q.; Wu, D. H.; Cao, A. Y.; Li, Z. H.; Cheng, Y.; Zheng, Q. S.; *et al.* Stretchable and Highly Sensitive Graphene-on-Polymer Strain Sensors. *Sci. Rep.* **2012**, *2*, 870.
17. Alamusi; Hu, N.; Fukunaga, H.; Atobe, S.; Liu, Y. L.; Li, J. H. Piezoresistive Strain Sensors Made from Carbon Nanotubes Based Polymer Nanocomposites. *Sensors* **2011**, *11*, 10691–10723.
18. Hu, N.; Karube, Y.; Arai, M.; Watanabe, T.; Yan, C.; Li, Y.; Liu, Y. L.; Fukunaga, H. Investigation on Sensitivity of a Polymer/Carbon Nanotube Composite Strain Sensor. *Carbon* **2010**, *48*, 680–687.
19. Chang, F. Y.; Wang, R. H.; Yang, H.; Lin, Y. H.; Chen, T. M.; Huang, S. J. Flexible Strain Sensors Fabricated with Carbon Nano-Tube and Carbon Nano-Fiber Composite Thin Films. *Thin Solid Films* **2010**, *518*, 7343–7347.
20. Hu, N.; Karube, Y.; Yan, C.; Masuda, Z.; Fukunaga, H. Tunneling Effect in a Polymer/Carbon Nanotube Nanocomposite Strain Sensor. *Acta Mater.* **2008**, *56*, 2929–2936.
21. Yin, G.; Hu, N.; Karube, Y.; Liu, Y. L.; Li, Y.; Fukunaga, H. A Carbon Nanotube/Polymer Strain Sensor with Linear and Anti-Symmetric Piezoresistivity. *J. Compos. Mater.* **2011**, *45*, 1315–1323.
22. Pham, G. T.; Park, Y. B.; Liang, Z.; Zhang, C.; Wang, B. Processing and Modeling of Conductive Thermoplastic/Carbon Nanotube Films for Strain Sensing. *Compos. Part B, Eng.* **2008**, *39*, 209–216.
23. Kim, Y. J.; Cha, J. Y.; Ham, H.; Huh, H.; So, D. S.; Kang, I. Preparation of Piezoresistive Nano Smart Hybrid Material

Based on Graphene. *Curr. Appl. Phys.* **2011**, *11*, S350–S352.

24. Eswaraiah, V.; Balasubramaniam, K.; Ramaprabhu, S. Functionalized Graphene Reinforced Thermoplastic Nanocomposites as Strain Sensors in Structural Health Monitoring. *J. Mater. Chem.* **2011**, *21*, 12626–12628.

25. Wang, Y.; Yang, R.; Shi, Z. W.; Zhang, L. C.; Shi, D. X.; Wang, E.; Zhang, G. Y. Super-Elastic Graphene Ripples for Flexible Strain Sensors. *ACS Nano* **2011**, *5*, 3645–3650.

26. Paleo, A. J.; van Hattum, F. W. J.; Pereira, J.; Rocha, J. G.; Silva, J.; Sencadas, V.; Lanceros-Mendez, S. The Piezoresistive Effect in Polypropylene-Carbon Nanofibre Composites Obtained by Shear Extrusion. *Smart Mater. Struct.* **2010**, *19*, 065013.

27. Cochrane, C.; Koncar, V.; Lewandowski, M.; Dufour, C. Design and Development of a Flexible Strain Sensor for Textile Structures Based on a Conductive Polymer Composite. *Sensors* **2007**, *7*, 473–492.

28. Mattmann, C.; Clemens, F.; Troster, G. Sensor for Measuring Strain in Textile. *Sensors* **2008**, *8*, 3719–3732.

29. Window, A. L. *Strain Gauge Technology*; Springer: Berlin, 1992.

30. Geim, A. K. Graphene: Status and Prospects. *Science* **2009**, *324*, 1530–1534.

31. Novoselov, K. S.; Fal'ko, V. I.; Colombo, L.; Gellert, P. R.; Schwab, M. G.; Kim, K. A Roadmap for Graphene. *Nature* **2012**, *490*, 192–200.

32. Hernandez, Y.; Nicolosi, V.; Lotya, M.; Blighe, F. M.; Sun, Z. Y.; De, S.; McGovern, I. T.; Holland, B.; Byrne, M.; Gun'ko, Y. K.; *et al.* High-Yield Production of Graphene by Liquid-Phase Exfoliation of Graphite. *Nat. Nanotechnol.* **2008**, *3*, 563–568.

33. Paton, K. R.; Varrla, E.; Backes, C.; Smith, R. J.; Khan, U.; O'Neill, A.; Boland, C.; Lotya, M.; Istrate, O. M.; King, P.; *et al.* Scalable Production of Large Quantities of Defect-Free, Few-Layer Graphene by Shear Exfoliation in Liquids. *Nat. Mater.* **2014**, *13*, 624–630.

34. Khan, U.; May, P.; O'Neill, A.; Coleman, J. N. Development of Stiff, Strong, yet Tough Composites by the Addition of Solvent Exfoliated Graphene to Polyurethane. *Carbon* **2010**, *48*, 4035–4041.

35. Coleman, J. N. Liquid Exfoliation of Defect-Free Graphene. *Acc. Chem. Res.* **2013**, *46*, 14–22.

36. Khan, U.; O'Neill, A.; Lotya, M.; De, S.; Coleman, J. N. High-Concentration Solvent Exfoliation of Graphene. *Small* **2010**, *6*, 864–871.

37. Unnikrishnan, G.; Thomas, S. Diffusion and Transport of Aromatic-Hydrocarbons through Natural-Rubber. *Polymer* **1994**, *35*, 5504–5510.

38. Frizzell, C. J.; in het Panhuis, M.; Coutinho, D. H.; Balkus, K. J.; Minett, A. I.; Blau, W. J.; Coleman, J. N. Reinforcement of Macroscopic Carbon Nanotube Structures by Polymer Intercalation: The Role of Polymer Molecular Weight and Chain Conformation. *Phys. Rev. B: Condens. Matter Mater. Phys.* **2005**, *72*, 245420.

39. Vahdat, N.; Sullivan, V. D. Estimation of Permeation Rate of Chemicals through Elastometric Materials. *J. Appl. Polym. Sci.* **2001**, *79*, 1265–1272.

40. Obasi, H. C.; Ogbobe, O.; Igwe, I. O. Diffusion Characteristics of Toluene into Natural Rubber/Linear Low Density Polyethylene Blends. *Int. J. Polym. Sci.* **2009**, *2009*, 140682.

41. Bird, R. B.; Stewart, W. E.; Lightfoot, E. N. *Transport Penomena*; John Wiley and Sons: New York, 1976.

42. Stauffer, D. S.; Aharony, A. *Introduction to Percolation Theory*; Taylor and Francis: London, 1994.

43. Cunningham, G.; Lotya, M.; McEvoy, N.; Duesberg, G. S.; van der Schoot, P.; Coleman, J. N. Percolation Scaling in Composites of Exfoliated Mos2 Filled with Nanotubes and Graphene. *Nanoscale* **2012**, *4*, 6260–6264.

44. Stankovich, S.; Dikin, D. A.; Dommett, G. H. B.; Kohlhaas, K. M.; Zimney, E. J.; Stach, E. A.; Piner, R. D.; Nguyen, S. T.; Ruoff, R. S. Graphene-Based Composite Materials. *Nature* **2006**, *442*, 282–286.

45. Garboczi, E. J.; Snyder, K. A.; Douglas, J. F.; Thorpe, M. F. Geometrical Percolation-Threshold of Overlapping Ellipsoids. *Phys. Rev. E: Stat. Phys., Plasmas, Fluids, Relat. Interdiscip. Top.* **1995**, *52*, 819–828.

46. De, S.; King, P. J.; Lotya, M.; O'Neill, A.; Doherty, E. M.; Hernandez, Y.; Duesberg, G. S.; Coleman, J. N. Flexible, Transparent, Conducting Films of Randomly Stacked Graphene from Surfactant-Stabilized, Oxide-Free Graphene Dispersions. *Small* **2010**, *6*, 458–464.

47. Finn, D. J.; Lotya, M.; Cunningham, G.; Smith, R. J.; McCloskey, D.; Donegan, J. F.; Coleman, J. N. Inkjet Deposition of Liquid-Exfoliated Graphene and Mos2 Nanosheets for Printed Device Applications. *J. Mater. Chem. C* **2014**, *2*, 925–932.

48. Bauhofer, W.; Kovacs, J. Z. A Review and Analysis of Electrical Percolation in Carbon Nanotube Polymer Composites. *Compos. Sci. Technol.* **2009**, *69*, 1486–1498.

49. Toki, S.; Che, J.; Rong, L.; Hsiao, B. S.; Amnuaypornsri, S.; Nimpaiboon, A.; Sakdapipanich, J. Entanglements and Networks to Strain-Induced Crystallization and Stress−Strain Relations in Natural Rubber and Synthetic Polyisoprene at Various Temperatures. *Macromolecules* **2013**, *46*, 5238–5248.

50. Yang, L. L.; Ge, Y.; Zhu, Q. H.; Zhang, C.; Wang, Z. P.; Liu, P. H. Experimental and Numerical Studies on the Sensitivity of Carbon Fibre/Silicone Rubber Composite Sensors. *Smart Mater. Struct.* **2012**, *21*, 035011.

51. Zhang, R.; Baxendale, M.; Peijs, T. Universal Resistivity-Strain Dependence of Carbon Nanotube/Polymer Composites. *Phys. Rev. B: Condens. Matter Mater. Phys.* **2007**, *76*, 195433.

52. Chen, L.; Chen, G. H.; Lu, L. Piezoresistive Behavior Study on Finger-Sensing Silicone Rubber/Graphite Nanosheet Nanocomposites. *Adv. Funct. Mater.* **2007**, *17*, 898–904.

53. Knite, M.; Teteris, V.; Kiploka, A.; Kaupuzs, J. Polyisoprene-Carbon Black Nanocomposites as Tensile Strain and Pressure Sensor Materials. *Sens. Actuators, A* **2004**, *110*, 142–149.

54. Shin, M. K.; Oh, J.; Lima, M.; Kozlov, M. E.; Kim, S. J.; Baughman, R. H. Elastomeric Conductive Composites Based on Carbon Nanotube Forests. *Adv. Mater. (Weinheim, Ger.)* **2010**, *22*, 2663–2667.

55. Zhang, R.; Deng, H.; Valenca, R.; Jin, J. H.; Fu, Q.; Bilotti, E.; Peijs, T. Strain Sensing Behaviour of Elastomeric Composite Films Containing Carbon Nanotubes under Cyclic Loading. *Compos. Sci. Technol.* **2013**, *74*, 1–5.

56. Conroy, J.; Verma, N. K.; Smith, R. J.; Rezvani, E.; Duesberg, G. S.; Coleman, J. N.; Volkov, Y. Biocompatibility of Pristine Graphene Monolayers, Nanosheets and Thin Films, **2014**; arXiv:1406.2497 [q-bio.CB].

57. Peliskova, M.; Piyamanocha, P.; Prokes, J.; Varga, M.; Saha, P. The Electrical Conductivity of Ethylene Butyl-Acrylate/Carbon Black Composites: The Effect of Foaming on the Percolation Threshold. *Synth. Met.* **2014**, *188*, 140–145.

58. Ezquerra, T. A.; Connor, M. T.; Roy, S.; Kulescza, M.; Fernandes-Nascimento, J.; Balta-Calleja, F. J. Alternating-Current Electrical Properties of Graphite, Carbon-Black and Carbon-Fiber Polymeric Composites. *Compos. Sci. Technol.* **2001**, *61*, 903–909.

59. Zhu, J. H.; Wei, S. Y.; Ryu, J.; Guo, Z. H. Strain-Sensing Elastomer/Carbon Nanofiber "Metacomposites". *J. Phys. Chem. C* **2011**, *115*, 13215–13222.

60. Ibarra, L.; Panos, D. Mechanical Properties of Thermoplastic Butadiene-Styrene (Sbs) and Oxidized Short Carbon Fibre Composites. *Polym. Int.* **1997**, *43*, 251–259.

61. Hindermann-Bischoff, M.; Ehrburger-Dolle, F. Electrical Conductivity of Carbon Black-Polyethylene Composites—Experimental Evidence of the Change of Cluster Connectivity in the Ptc Effect. *Carbon* **2001**, *39*, 375–382.

62. Jager, K. M.; McQueen, D. H.; Tchmutin, I. A.; Ryvkina, N. G.; Kluppel, M. Electron Transport and Ac Electrical Properties of Carbon Black Polymer Composites. *J. Phys. D: Appl. Phys.* **2001**, *34*, 2699–2707.

63. Li, F. K.; Qi, L. Y.; Yang, J. P.; Xu, M.; Luo, X. L.; Ma, D. Z. Polyurethane/Conducting Carbon Black Composites: Structure, Electric Conductivity, Strain Recovery Behavior; and Their Relationships. *J. Appl. Polym. Sci.* **2000**, *75*, 68–77.

64. Yi, W. J.; Wang, Y. Y.; Wang, G. F.; Tao, X. M. Investigation of Carbon Black/Silicone Elastomer/Dimethylsilicone Oil Composites for Flexible Strain Sensors. *Polym. Test.* **2012**, *31*, 677–684.

65. Khan, U.; Porwal, H.; O'Neill, A.; Nawaz, K.; May, P.; Coleman, J. N. Solvent-Exfoliated Graphene at Extremely High Concentration. *Langmuir* **2011**, *27*, 9077–9082.